

Correlation between color changes in Jupiter's storm "Oval BA", cloud heights and ultraviolet exposure

Tejoram Vivekanandan, Coimbatore Institute of Technology

Mentor: Glenn Orton, Jet Propulsion Laboratory

Co-Mentor: Thomas Momary, Jet Propulsion Laboratory

Abstract

Oval BA is the second largest anticyclonic vortex on Jupiter's surface, the largest being the Great Red Spot. Oval BA formed in 2000 and exhibited quasi periodic color changes over the years. Its initial white color started to change in November 2005 and became completely red in December 2005. Then, its red color was sustained for more than a decade. In July 2018, it was observed that its red color was fading. It turned completely white in December 2018 and stayed white for a couple of years. In recent observations from 2021, Oval BA is changing back to a faint red or pink again. To determine the correlation between these color changes and both the altitude and ultraviolet exposure of the storm's particles, near-infrared images of Jupiter showing Oval BA were examined. After calibration and preprocessing, images from the red, white, and transition phases were compiled for different wavelengths. The reflectivity of the vortex at each wavelength was corrected for its dependence on the angles of emission and incident sunlight using the Minnaert function. Results indicate a behavior consistent with a change in the altitude of particles between the red and white phases.

Introduction

Jupiter is the largest planet in the solar system. It has no solid surface. The atmosphere is filled with various cyclonic and anti-cyclonic vortices - storms rotating in the same or opposite direction as the planet. One such anti-cyclonic storm is Oval BA, located in Jupiter's southern hemisphere. The latitude of the storm is relatively constant, near 33°S planetocentric latitude, but the longitude of the vortex is not constant due to drift in Jupiter's turbulent atmosphere. The size of Oval BA is large enough to comfortably swallow the Earth. Oval BA formed in 2000 as a result of the merger of three smaller white storms. It was initially the same white color as the smaller storms. However, in December 2005, Oval BA changed from white to red during a period when it was not observable due to its proximity to the sun. It remained this color for a little more than a decade [1]. In July 2018, observers noted that Oval BA's red color was fading [2]. By December 2018, after Jupiter's solar conjunction, it was observed that Oval BA had once again become white [2]. Therefore, the purpose of this study is to determine whether these color changes are associated with any change in the altitude of the particles within Oval BA.

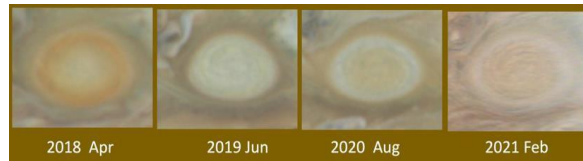


Figure 1. Changes of color of the anticyclone Oval BA. (Left) Red color Oval BA observed in April 2018. (Middle Left) White color Oval BA observed in June 2019. (Middle Right) Transition of white to Pink Oval BA observed in August 2020. (Right) Pink color Oval BA observed in February 2021.

Methods

Image collection and calibration

This project collects images from the SpeX instrument at NASA's InfraRed Telescope Facility (IRTF) and the Near-InfraRed Imager (NIRI) at the Gemini North Telescope. Both facilities are at the summit of the ~14,000 foot Maunakea, Hawaii. The images provided by both instruments cover the spectral range between 1.58 and 2.26 μm . Any unprocessed image in IR observation would be highly affected by sky background emission. This situation is similar to trying to view stars during the daylight at visible wavelengths. To avoid this, we would use the Nodding technique, which subtracts a nearby sky background image from the Jupiter image. Figure 2 represents examples of the Nodding technique.

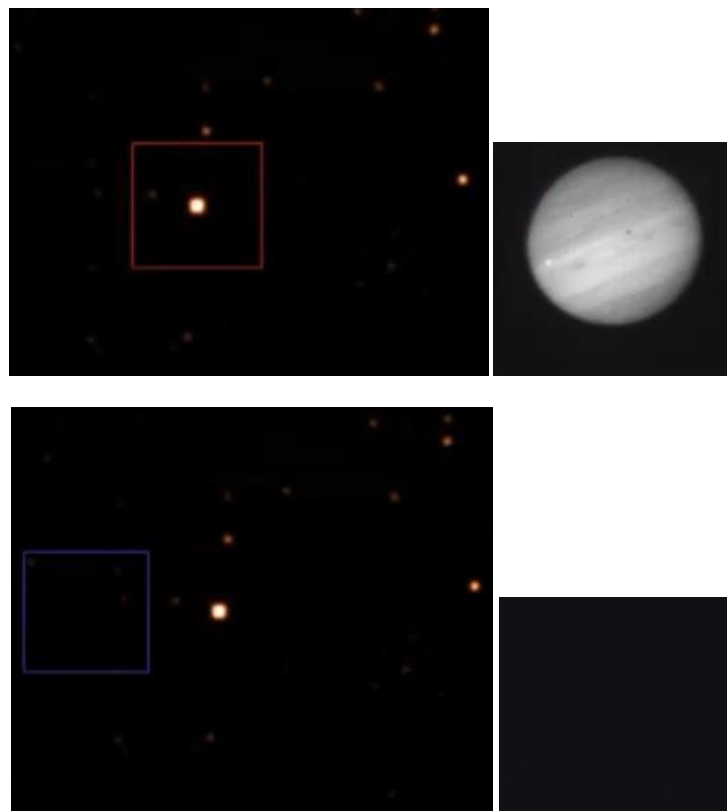


Figure 2. (Top) On source image. (Bottom) Off source image. The top right image shows Jupiter while on source. The bottom right image shows background sky while off source.

Image Compilation and Sorting

Jupiter was imaged using several discrete filters at near-infrared wavelengths sensitive to reflected sunlight from clouds at various levels in Jupiter's upper troposphere and lower stratosphere. Images were selected in which Oval BA was visible. The selected images were taken at various wavelengths and include epochs when Oval BA is visibly red, white, and the transition follows.

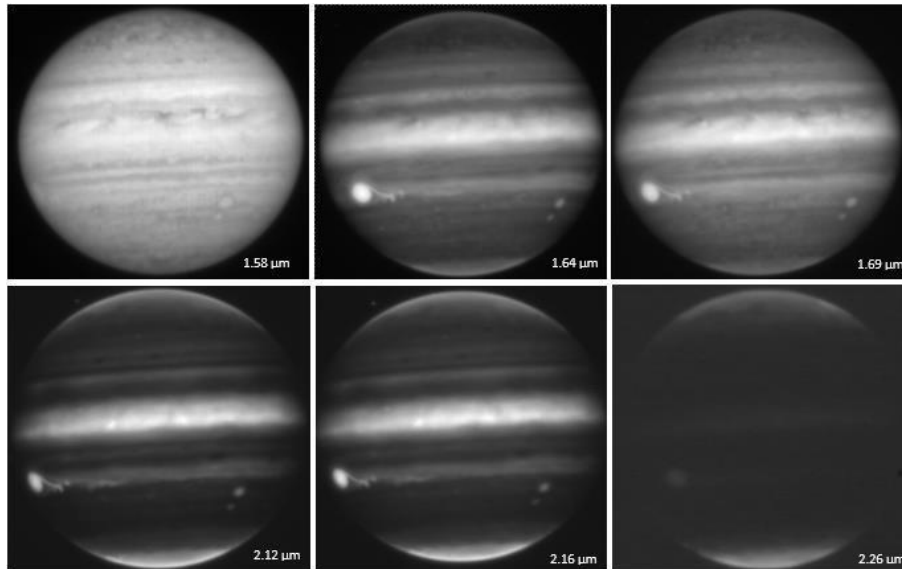


Figure 3. Images taken using the SpeX instrument's "Guide Dog" camera on Jun 3, 2019, at various wavelengths. Oval BA is recognizable as the brighter oval near the "4-o'clock" position of these images.

After this compilation process, the images are sorted based on their respective wavelengths as a function of time to determine if there are any visible changes present in Oval BA's surroundings or morphology. The SpeX filters in which images are compiled include the short absorption band of methane (1.58 μm), iron II (1.64 μm), long absorption bands of methane (1.69 μm), hydrogen 1-0 (2.12 μm), bracket gamma (2.16 μm), and continuum-K (2.26 μm). The NIRI filters in which images are compiled include the short and long absorption bands of methane, bracket gamma, hydrogen, H₂O-ice (2.05 μm), and methane-ice (2.28 μm). Figure 3 shows examples of IRTF SpeX images with oval BA present. Subsequently, these images are converted into cylindrical maps.

Central-Meridian Plots

Next, central-meridian strips are extracted from the previously created cylindrical maps to check the consistency of the image set's reflectivity and verify whether any discrete feature, such as the Great Red Spot or a bright satellite, had compromised the accuracy of the initial calibration process (achieved by averaging over the Earth-facing hemisphere).

To make the central meridian plots, images are grouped by wavelength, and an input file of relevant images is created for each wavelength. Next, central-meridian strips are extracted from the cylindrical maps and plotted as a line graph. If any images have central-meridian strips that deviate significantly from the norm, these images are removed from the input file and added to a new input file containing all outliers for that wavelength. Finally, an average central-meridian strip, excluding the outlier data, is plotted. The outlier images are then re-adjusted and re-calibrated to be more consistent with the mean and are returned to the original input file to create a more accurate central-meridian plot.

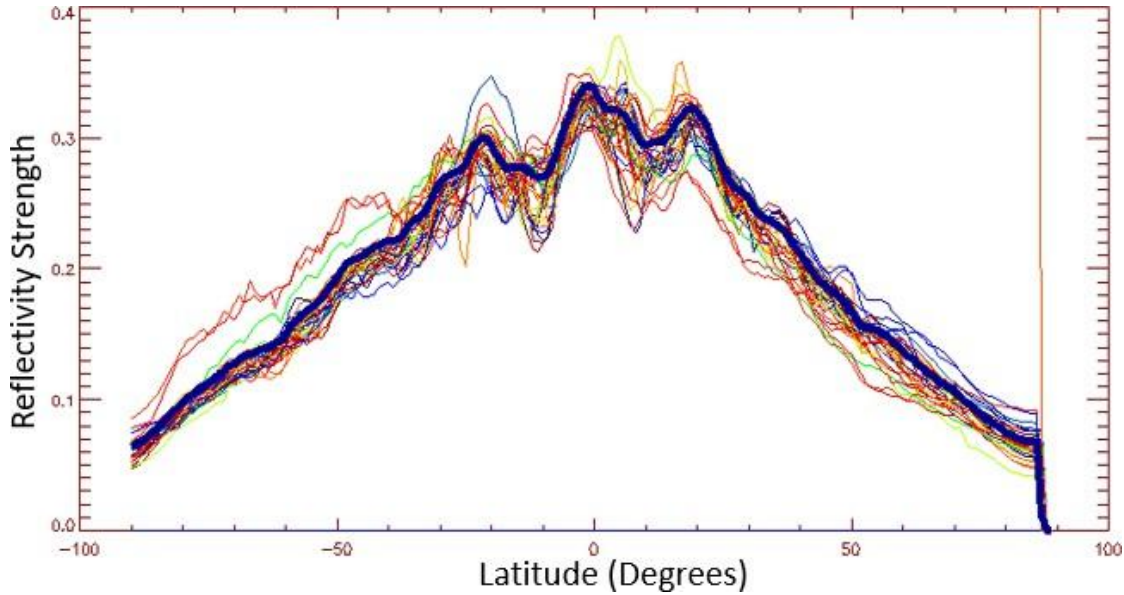


Figure 4. A composite central meridian plot of images at a wavelength of 1.58 microns.

The Minnaert Function

The dependence of the observed reflectivity from a planet's location on the incidence and emission angles can be approximated using the Minnaert function [4]. This empirical law was first introduced by Marcel Minnaert in 1941. For an observation at a specific wavelength, one can approximately calculate the observed reflectivity (I/F) as:

$$\frac{I}{F} = \left(\frac{I}{F}\right)_0 \cdot \mu_0^k \cdot \mu^{k-1} \quad (\text{Eq. 1})$$

where $(I/F)_0$ is the nadir-viewing reflectivity of the selected point, k is the limb-darkening parameter, μ is the cosine of the emission angle at that point, and μ_0 is the cosine of the solar incidence angle at the same point [4]. After taking the logarithms of both sides of this equation and performing algebraic manipulations, the equation can be rewritten as:

$$\ln(\mu \times (I/F)) = \ln((I/F)_0) + k \times \ln(\mu \times \mu_0) \quad (\text{Eq. 2})$$

Using this form of the equation, it is possible to emulate a linear regression line in slope intercept form ($y = m \cdot x + b$) where $y = \ln(\mu \cdot (I/F))$, $m = k$, $x = \mu \cdot \mu_0$, and $b = \ln((I/F)_0)$. Thus, it is possible to fit the Minnaert parameters $(I/F)_0$ and k using a least-squares fit on a set of $\ln(\mu \cdot (I/F))$ as a function of $(\mu \cdot \mu_0)$ [4]. It is this linearized form of the Minnaert function that is plotted in the figures below.

After final-stage calibrations have been completed, images in which Oval BA was barely visible, blurry, or too close to either limb of the planet are removed from the datasets to improve the overall quality of the data being considered. First, using cylindrical maps, the coordinates of the center of Oval BA are determined. Next, an averaged version of the I/F value is computed using these coordinates. This averaged approach produces more reliable values than the single-pixel computation method by increasing stability. The kernel size used to compute the average value depends entirely on the size of Oval BA in the respective image. The distance between Earth and Jupiter is constantly changing due to planetary motion. As our observations were made using ground-based telescopes, it is important to consider this change in distance. Figure 5 shows the distance between Earth and Jupiter measured in astronomical units over the years. Obviously, with changes in distance, the apparent size of Oval BA in the image changes irrespective of any change in the actual size of Oval BA. Thus, in our computation, the kernel size is fixed with respect to the distance on the date of observation.

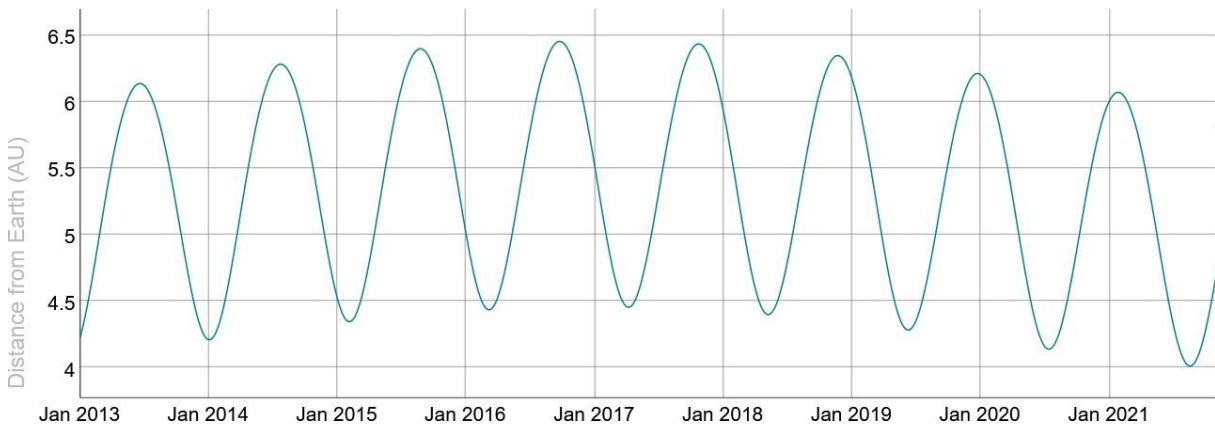


Figure 5. Distance of Jupiter from earth measured in astronomical unit (AU).

Similarly, μ and μ_0 values are determined using each cylindrical map's respective *.mu and *.mu0 files. Also, I/F values are determined at longitudes on either side of Oval BA, which we termed as West I/F and East I/F . These values are then documented in a separate table characterized by the image's wavelength and epoch ("red" or "white").

After these values are compiled, they are plotted. Next, a line of best fit is generated, and the uncertainty of the data is recorded.

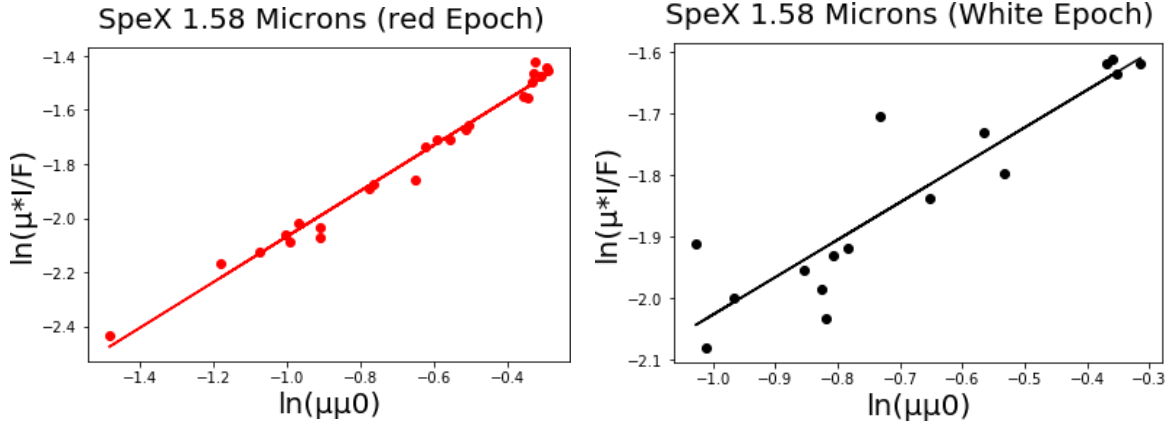


Figure 6. (Left) A plot of the reflectivity (y-axis) as a function of emission and incident angle cosines (x-axis) during the red epoch of Oval BA in SpeX observations. (Right) A plot of the reflectivity (y-axis) as a function of emission and incident angles (x-axis) during the white epoch of Oval BA in SpeX observations.

These two plots are then combined to see if there exists a different pattern of reflectivity values for the two different epochs of Oval BA. This process is repeated for each of the SpeX and NIRI filters.

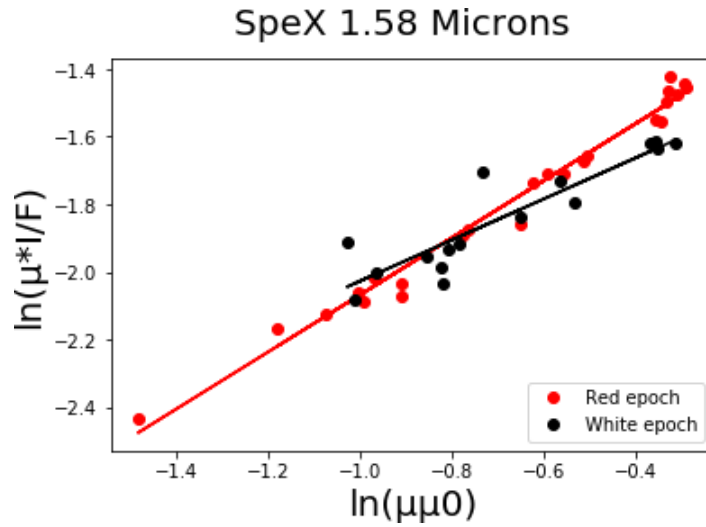


Figure 7. A plot of reflectivity as a function of emission and incident angles of both the red and white epochs of SpeX observations overlaid against each other.

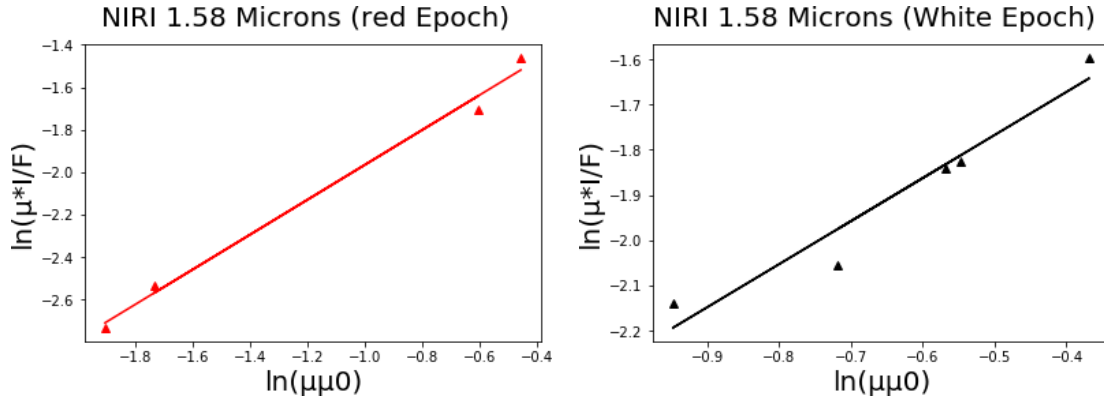


Figure 8. Plots of the reflectivity (y-axis) measured for NIRI images as a function of emission and incident angles (x-axis): Left during the red epoch of Oval BA: Right during the white epoch of Oval BA

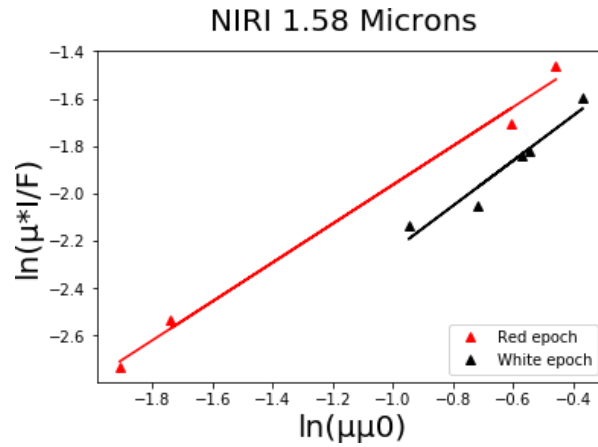


Figure 9. A plot of reflectivity as a function of emission and incident angles of both the red and white epochs of NIRI observations overlaid against each other.

In addition, SpeX and NIRI filters that cover the same wavelength are combined to see if their reflectivity patterns are consistent during both epochs. At the wavelengths that contain both SpeX and NIRI observations, the combined data of the red and white epochs are over-plotted for further comparisons between the two epochs.

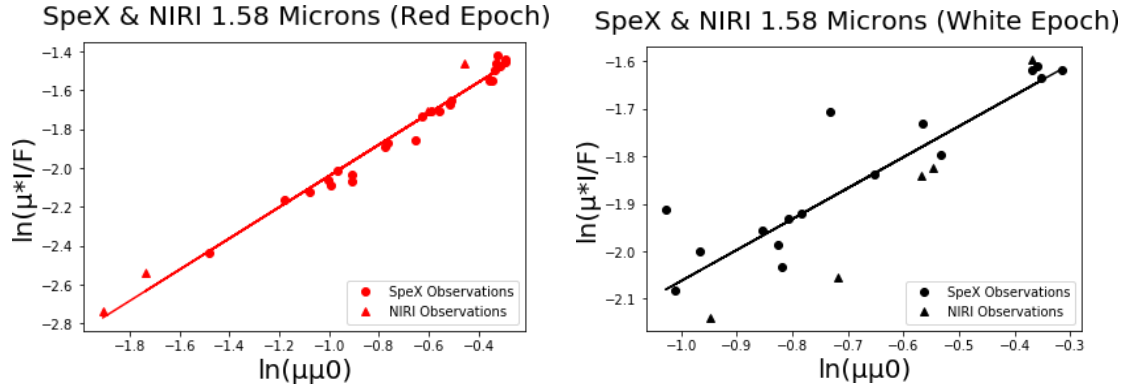


Figure 10. (Left) A combined plot of SpeX and NIRI observations in the red epoch taken using the methane short band filter (1.58 μm). (Right) A combined plot of SpeX and NIRI observations in the white epoch taken using the methane short band filter (1.58 μm).

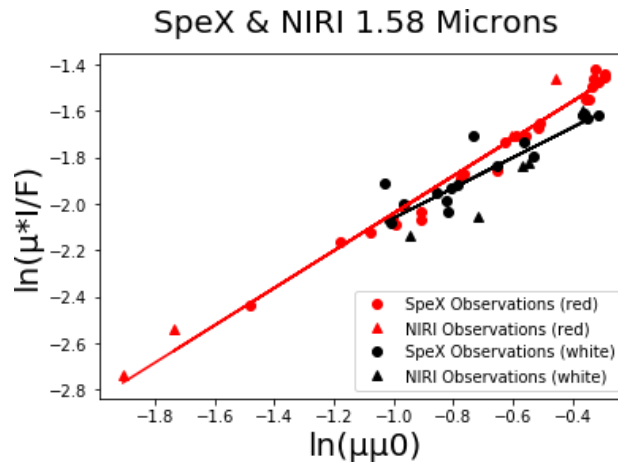


Figure 11. A plot of the reflectivity as a function of emission and incident angles of both the red and white epochs of SpeX and NIRI observations overlaid against each other using the methane short band filter (1.58 μm).

Using the uncertainties for the slope and y-intercept for the lines of best fit for both epochs, it is possible to create a confidence interval for each epoch's observed reflectivity to view the difference in I/F values. To do this, the largest product of a pair of μ and μ_0 values in the epoch is selected to ensure that that specific point on the x-axis ($(\mu\mu_0)$) contains overlapping data for both epochs without fear of extrapolation. This value of μ , in addition to the confidence intervals for the slope and y-intercept for each epoch, can be substituted into the linear regression form of the Minnaert equation. The confidence interval for the observed reflectivity is achieved by solving for I/F using this equation. After calculating the confidence interval of the reflectivity for both the red and white epochs, it is possible to compare these values to see if there is enough certainty that a change in reflectivity occurred when Oval BA went through its transformation of red to white.

Results

Our goal was to determine whether there were any changes in the properties of particles in the atmosphere, diagnosed by changes in their near-infrared reflectivity, that could be diagnostic of changes in the particle properties, particularly altitude. If the reddening of Oval BA particles is the result of solar ultraviolet irradiation that increases with particle altitude, then is the return to white-colored particles the result of drop in the particle altitude? This would be diagnosed by lower reflectivity in spectral regions with strong gaseous absorption, which is what is being looked for.

Most of the comparisons of reflectivity were summarized by using the Minnaert function to fit the reflectivity of Oval BA as a function of the cosine of the incident and emission angles. This was important because individual measurements of Oval BA when it was white and when it was red never matched with identical values of the incident and emission angles.

The results of these fits are plotted using a linear fit of the Minnaert function described above in Equations 1 and 2. The logarithmic form (Eq. 2) is what is plotted in Figures 12-20. After all the data are plotted for each wavelength, a line of best fit is generated with uncertainty values for its slope and y-intercept for the values corresponding to both red and white epochs. Then, these two lines are overlaid against each other to be able to compare their respective observed μ^*I/F values relative to each other.

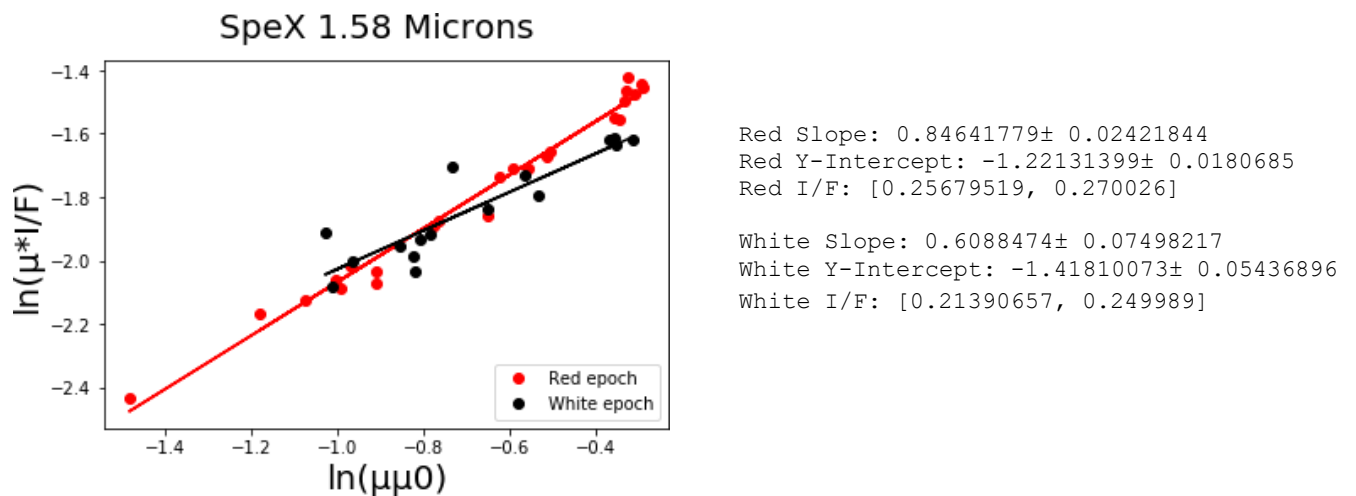


Figure 12. A plot of the reflectivity as a function of emission and incident angles of SpeX observations of both the red and white epochs overlaid against each other at 1.58 μm (methane_short filter). The x-axis represents the logarithm of product of the emission and incident angle cosines and the y-axis represents the logarithm of the product of the reflectivity at that angle times the emission-angle cosine. Values for the slope and intercept of the fit are shown together with their respective uncertainties, along with the I/F range representing the confidence interval at the maximum value of the product of μ and μ_0 .

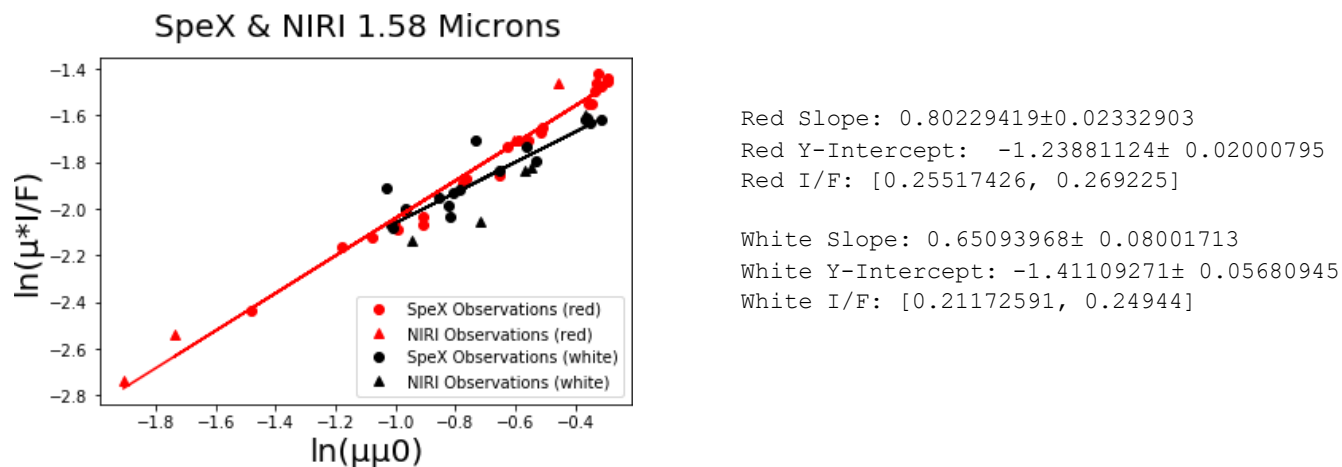


Figure 13. A plot of the same data as in Fig. 12 but with the combination of NIRI and SpeX measurements.

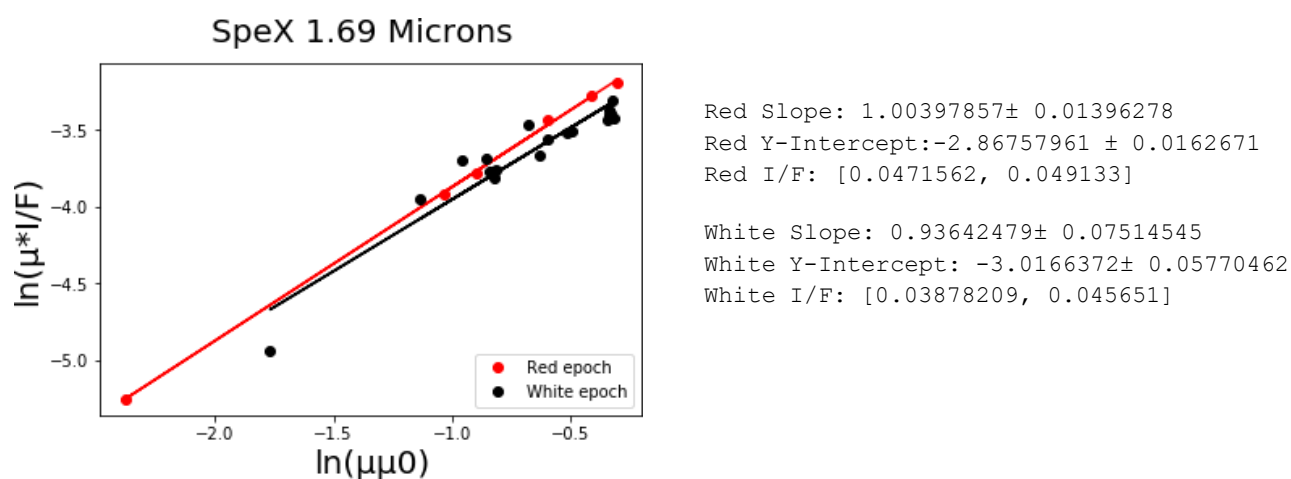
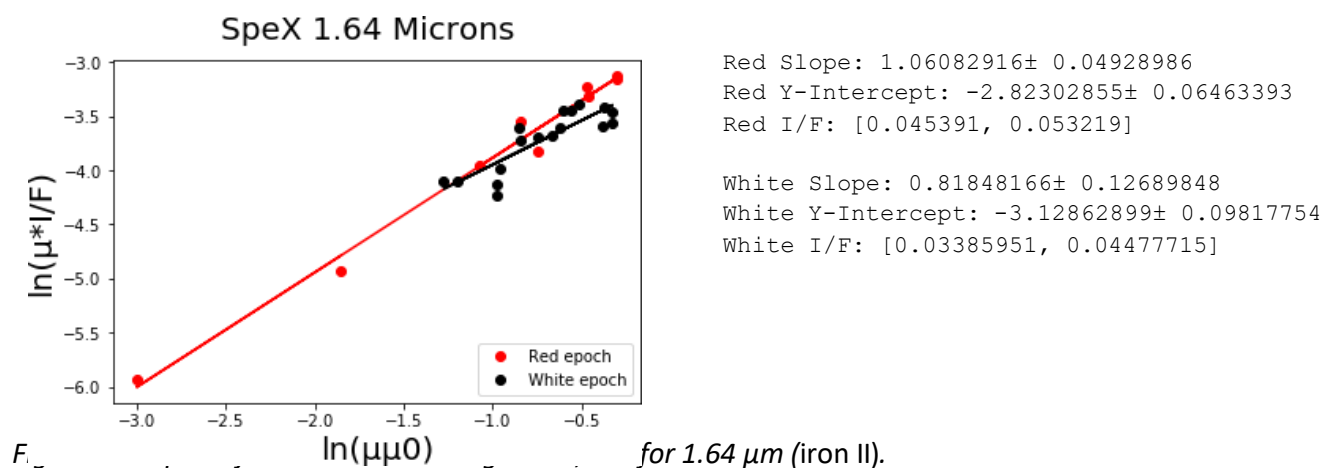
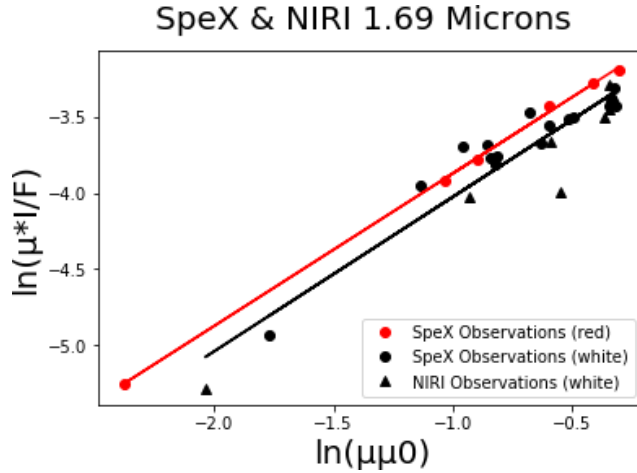
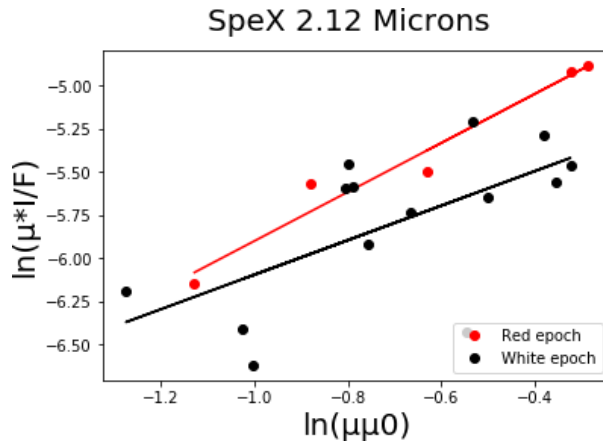


Figure 15. A plot of values like Figure 12, but for $1.69 \mu\text{m}$ (methane_long filter).



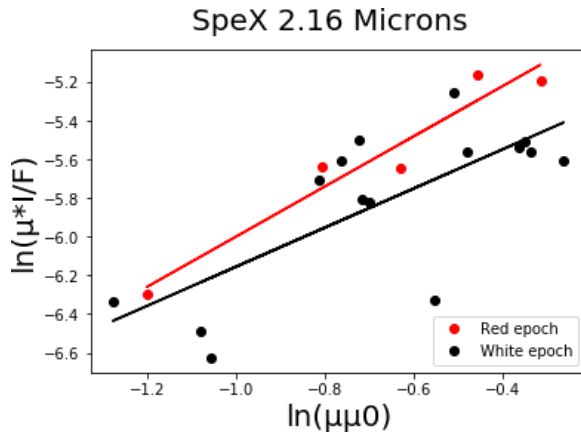
Red Slope: $1.00397857 \pm 0.01396278$
 Red Y-Intercept: $-2.86757961 \pm 0.0162671$
 Red I/F: [0.0471562, 0.049133]
 White Slope: 1.01628559 ± 0.0700657
 White Y-Intercept: $-3.00958499 \pm 0.05703948$
 White I/F: [0.03816652, 0.044723]

Figure 16. A plot of values like Figure 13, but for 1.69 μm (methane_long filter).



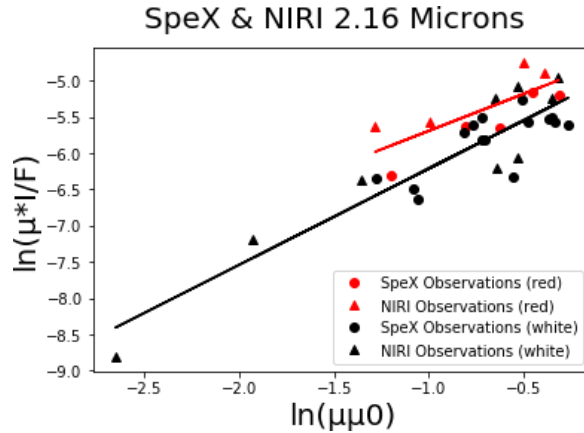
Red Slope: $1.42600573 \pm 0.17389225$
 Red Y-Intercept: $-4.4765554 \pm 0.12617675$
 Red I/F: [0.007229, 0.01029]
 White Slope: $1.00432517 \pm 0.36469462$
 White Y-Intercept: $-5.09312947 \pm 0.27242739$
 White I/F: [0.003491, 0.007631]

Figure 17. A plot of values like Figure 12, but for 2.12 μm (H_2 1-0 filter).



Red Slope: $1.29598698 \pm 0.19718198$
 Red Y-Intercept: $-4.70374829 \pm 0.14747455$
 Red I/F: [0.00558296, 0.008489]
 White Slope: 1.01067318 ± 0.2637717
 White Y-Intercept: $-5.14465411 \pm 0.19168533$
 White I/F: [0.00391525, 0.006599]

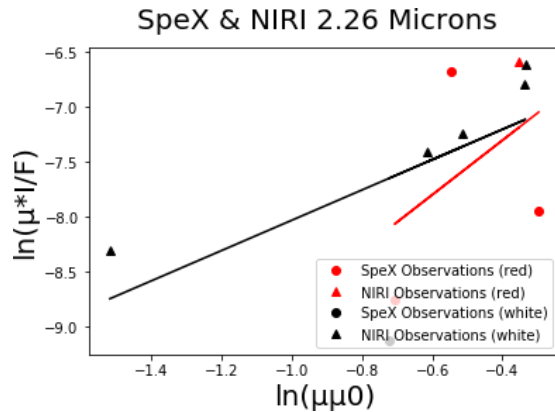
Figure 18. A plot of values like Figure 12, but for 2.16 μm (bracket_gamma filter).



Red Slope: $1.02041088 \pm 0.31069051$
 Red Y-Intercept: $-4.67276538 \pm 0.25043442$
 Red I/F: $[0.00546698, 0.010969]$

White Slope: $1.32781995 \pm 0.13152863$
 White Y-Intercept: $-4.8856821 \pm 0.12628794$
 White I/F: $[0.00515853, 0.007116]$

Figure 19. A plot of values like Figure 13, but for 2.16 μm (bracket_gamma filter).



Red Slope: 2.47980977 ± 3.5342026
 Red Y-Intercept: $-6.31110439 \pm 1.77739889$
 Red I/F: $[0.0000595766662, 0.0169554478]$

White Slope: $1.37737603 \pm 0.84091832$
 White Y-Intercept: $-6.65247352 \pm 0.65965546$
 White I/F: $[0.000373, 0.002448]$

Figure 20. A plot of values like Figure 13, but for 2.26 μm (continuum-K).

Conclusions

At 1.58 μm , tropospheric water-ammonia clouds are detectable at pressures greater than or equal to 700 mbar. Reflectivity at this wavelength is sensitive to the reflectivity of the cloud particles. The confidence interval for the observed reflectivity for the red epoch of the combined SpeX and NIRI observations is $[0.25517426, 0.269225]$ and for the white epoch is $[0.21172591, 0.24944]$. Thus, there is a small but still significant difference between the two epochs at this wavelength that is evident at the highest values of $\ln(\mu\mu_0)$. So, it can be concluded that there exists a change in observed reflectivity in correlation to the color change of Oval BA in the 1.58-micron filter.

The 1.64- and 1.69- μm filters sense regions of intermediate gaseous absorption. At these wavelengths, high tropospheric haze cloud particles are detectable near 200 mbars of pressure. At low emission angles (high x-axis values) at these wavelengths, the y-values for the red epoch are consistently higher

than the y values for the white epoch. The confidence interval for the observed reflectivity for the red epoch at 1.64 microns is [0.045391, 0.053219] and for the white epoch is [0.03385951, 0.04477715]. Once again, there is no overlap in confidence intervals. The confidence interval for the observed reflectivity for the red epoch of combined SpeX and NIRI observations at 1.69 μm is [0.0471562, 0.049133] and for the white epoch is [0.03816652, 0.044723]. There is a huge difference in confidence intervals. Hence, there is a difference between the two epochs at 1.69 microns. Therefore, the white epoch of Oval BA has a lower reflectivity of high-altitude hazes, implying that in the white epoch, Oval BA's clouds are lower in altitude compared to its red epoch.

The 2.12- and 2.16- μm filters sense stronger gaseous absorption and are sensitive to particles even higher – in the lower stratosphere around 80-100 mbars of pressure. The confidence interval at 2.12 μm SpeX for the red epoch is [0.007229, 0.01029] and for the white epoch is [0.003491, 0.007631]. Since there is small but still considerable overlap between these two intervals, it cannot be concluded that there exists a change in reflectivity at this filter. The confidence interval at 2.16 microns combined SpeX and NIRI for the red epoch is [0.00546698, 0.010969] and for the white epoch is [0.00515853, 0.007116]. Once again, since there is significant overlap between these two intervals, it cannot be concluded that there exists a change in reflectivity at the 2.16-micron filter. The same holds good for 2.26 μm . Thus, we do not know if a change occurred in the vertical distribution of haze particles in Oval BA during its red to white transition in the lower stratosphere.

To summarize, because of Oval BA's color change from red to white, Oval BA has different cloud properties in the upper troposphere, roughly at 200 mbar of pressure or more but not in the lower stratosphere at pressures of 80-100 mbar.

Acknowledgments

Thank you to mentor Glenn Orton and co-mentor Thomas Momary at the Jet Propulsion Laboratory, California Institute of Technology for their guidance and support in this research. Thank you to JPL Visiting Student Research Program and JPL Education Office - Student & Faculty Programs for the opportunity. Lastly, thank you to everyone who has provided support and guidance for the research.

References

- [1] Baines, K. H., R. A. West, L. P. Giver, and F. Moreno. 1993. Quasi-random narrow band model fits to near-infrared low-temperature laboratory methane spectra and derived exponential-sum absorption coefficients. *J. Geophys. Res. - Planets* 98, E3, 5517-5529.
- [2] Reuter, D. C., A. A. Simon-Miller, A. Lunsford, K. H. Baines, A. F. Cheng, D. E. Jennings, C. B. Olkin, J. R. Spencer, S. A. Stern, H. A. Weaver, and L. A. Young. 2007. Jupiter cloud composition, stratification, convection, and wave motion: A view from New Horizons. *Science* 318, 223-225.

[3] Irwin, P.G.J., N.A. Teanby, R. de Kok, L.N. Fletcher, C.J.A. Howett, C.C.C. Tsang, C.F. Wilson, S.B. Calcutt, C.A. Nixon, P.D. Parrish. 2008. The NEMESIS planetary atmosphere radiative transfer and retrieval tool, *J. Quant. Spectrosc. and Rad. Trans.*, 109, 1136-1150.

[4] Irwin, P.G.J., Dobinson, J, James A, Toledo D, Teanby N.A., Fletcher, L.N., Orton G.S., Perez -Hoyos, S. Latitudinal variation of methane abundance above 2 clouds in Neptune's atmosphere from 3 VLT/MUSE-NFM: Limb-darkening reanalysis. *Icarus*